nature communications

Article

https://doi.org/10.1038/s41467-026-70184-x

Long-range magnetic order with disordered spin orientations in a high-entropy antiferromagnet

Received: 7 June 2025

Accepted: 17 February 2026

Published online: 06 March 2026

Check for updates

Yao Shen[1,2] ✉, Guangkai Zhang[1,3], Qinghua Zhang[1], Xuejuan Gui[4,5], Yu Zhang[1], Heemin Lee[6], Cheng-Tai Kuo[6], Jun-Sik Lee[6], Ronny Sutarto[7], Feng Ye[8], Zhao Pan[1], Xiaomei Qin[3], Jinchen Wang[4,5,9,10] ✉, Tianping Ying[1] ✉ & Youwen Long[1,2]

Disorder in magnetic systems typically suppresses long-range order, promoting short-range states such as spin glasses and magnetic clusters. This is particularly prominent in high-entropy materials, characterized by the random distributions of local magnetic entities and exchange interactions. However, in rare exceptions, long-range magnetic order can persist in high-entropy systems, while the microscopic characters and underlying mechanisms remain elusive, especially the magnetic behaviors of individual elements. Here, combining neutron diffraction and resonant soft x-ray scattering, we have conducted an element-specific investigation into the magnetic order of a high-entropy honeycomb-lattice van der Waals material $(Mn_{1/4}Fe_{1/4}Co_{1/4}Ni_{1/4})PS_3$. Despite significant atomic disorder, long-range zigzag antiferromagnetic order is observed below 72 K, with all four transition-metal elements participating in a unified phase transition. However, the spin orientations of various elements are distinct, attributed to the competition between single-ion anisotropies and exchange interactions. Our findings showcase a novel form of long-range magnetic order with disordered spin orientations, which is synergically stabilized by distinct magnetic elements in a high entropy magnet, offering a new paradigm for understanding complex magnetic systems.

Conventionally, magnetism is characterized by order parameters indicative of symmetry breaking and features a repeating pattern of magnetic moments. Disorder can be introduced through chemical substitution, which is commonly treated as local perturbations when its effects are weak. However, when disorder becomes significant—such as when dopant concentrations approach those of the host material—the periodic spin arrangement can be entirely disrupted, leading to dramatically weakened magnetic correlations. In classical magnetic systems, such disordered states with short-range order are generally understood within the framework of spin glass theory[1,2].

Such is the case for the magnetism in high-entropy (HE) materials —such as alloys[3–7], ceramics[8], oxides[9,10], and van der Waals

[1]Beijing National Laboratory for Condensed Matter Physics, Institute of Physics, Chinese Academy of Sciences, Beijing, China. [2]School of Physical Sciences, University of Chinese Academy of Sciences, Beijing, China. [3]Department of Physics, Shanghai Normal University, Shanghai, China. [4]Laboratory for Neutron Scattering, School of Physics, Renmin University of China, Beijing, China. [5]Key Laboratory of Quantum State Construction and Manipulation (Ministry of Education), Renmin University of China, Beijing, China. [6]Stanford Synchrotron Radiation Lightsource, SLAC National Accelerator Laboratory, Menlo Park, CA, USA. [7]Canadian Light Source, Saskatoon, SK, Canada. [8]Neutron Scattering Division, Oak Ridge National Laboratory, Oak Ridge, TN, USA. [9]PSI Center for Neutron and Muon Sciences, Villigen, PSI, Switzerland. [10]Laboratory for Quantum Magnetism, Institute of Physics, École Polytechnique Fédérale de Lausanne (EPFL), Lausanne, Switzerland. ✉e-mail: yshen@iphy.ac.cn; jcwang_phys@ruc.edu.cn; ying@iphy.ac.cn

https://doi.org/10.1038/s41467-026-70184-x

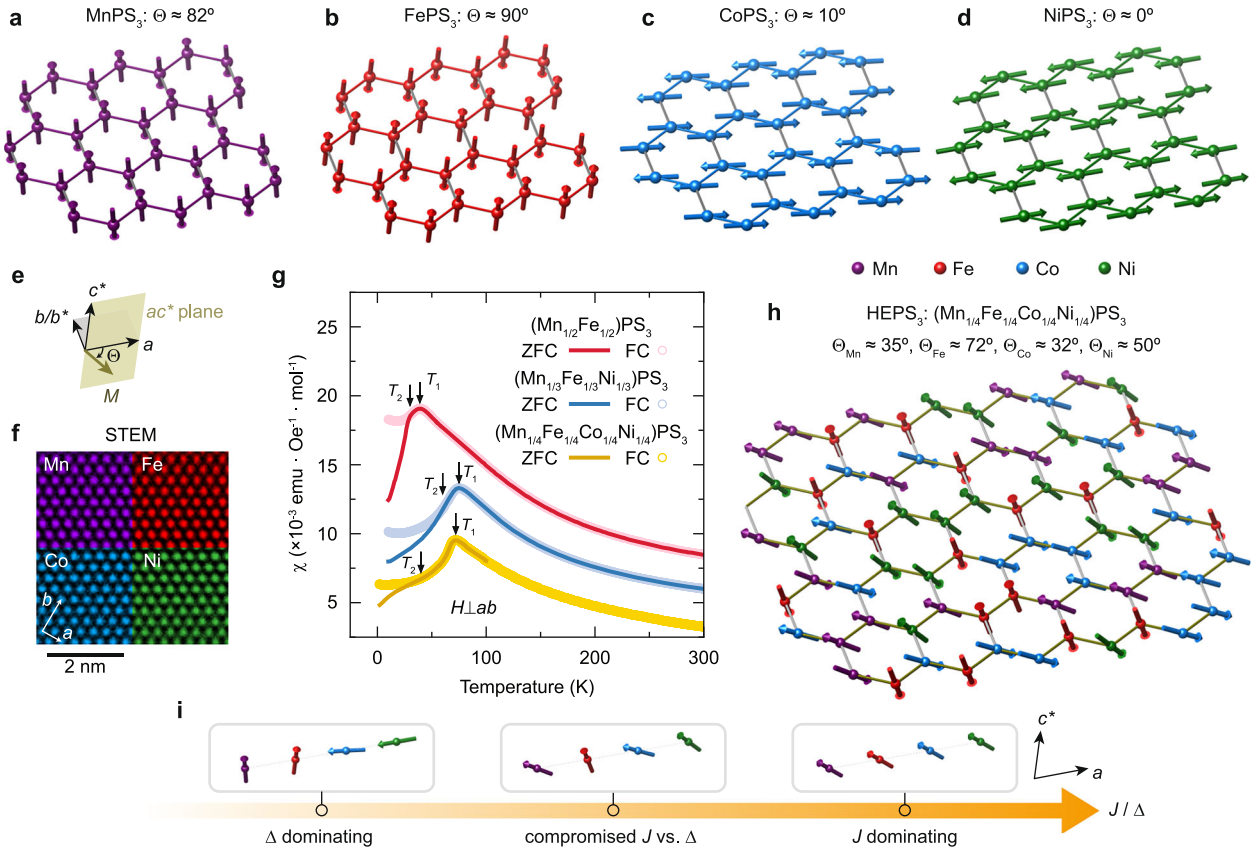

Fig. 1 | Magnetic properties of $TMPX_3$ and $HEPS_3$. a–d Schematics of the magnetic structure of $MnPS_3$, $FePS_3$, $CoPS_3$, and $NiPS_3$, respectively. All spin moments lie within the ac^* plane. **e** We define Θ as the angle between the spin moment **M** and lattice **a** direction. **f** Atomic-resolved elemental scanning transmission electron microscopy (STEM) mapping of $HEPS_3$, demonstrating the random distributions of various elements. **g** Magnetic susceptibility of $HEPS_3$ and other derivatives of $TMPX_3$ measured in the zero-field-cooling (ZFC) and field-cooling (FC) modes, respectively. For each material, the susceptibility exhibits an anomaly at T_1, and the ZFC and FC profiles split below T_2. **h** Schematic of the magnetic structure of $HEPS_3$ determined from neutron diffraction and RSXS measurements. **i**, Schematic diagram showing the evolution of spin orientations with different exchange interaction (J) to single-ion anisotropy (Δ) ratio. When J is negligible, the spin moments tend to preserve their anisotropy as in the non-HE materials, e.g., Mn^{2+}/Fe^{2+} and Co^{2+}/Ni^{2+} being almost perpendicular and parallel to the ab plane, respectively (left panel). In another aspect, dominant J would enforce a universal parallel alignment (right panel). A compromised case is realized in $HEPS_3$ (middle panel, see also Supplementary Note 6).

compounds[11–13]. These materials feature multiple principal elements randomly distributed at comparable concentrations, yielding exceptionally high configurational entropy. They can exhibit highly tunable properties, novel topological electronic structures[14], and outstanding performance in applications[15–17]. Regarding magnetic properties, the substantial disorder arising from randomly distributed magnetic moments and exchange interactions is expected to suppress long-range magnetic order. Indeed, glass-like magnetic behaviors are commonly observed in HE magnets[18,19], where spin moments are frozen in random directions, pinned by local lattice distortions. Yet, in some rare cases, long-range magnetic order can persist[20–23], presenting a fundamental paradox given the inherent disorder of the system, and the nature of such ordering remains unresolved. For instance, it is often presumed that once magnetic order is established in HE magnets, it uniformly affects all constituent elements with identical transition temperatures and spin orientations, even though each element, with its distinct orbital filling, could contribute its unique magnetic characteristics such as spin magnitudes and single-ion anisotropies. In fact, the magnetic behaviors of individual magnetic elements have never been thoroughly explored in HE materials. The lack of HE single crystals poses an additional barrier for detailed studies of their magnetic properties.

In this regard, $HEPS_3$, short for $(Mn_{1/4}Fe_{1/4}Co_{1/4}Ni_{1/4})PS_3$, emerges as a pivotal candidate to address this gap[11]. As a newly discovered HE van der Waals material, it features a slightly distorted two-dimensional (2D) honeycomb lattice with the monoclinic space group $C2/m$ and lattice constants of $a = 5.9321$ Å, $b = 10.2737$ Å, $c = 6.7061$ Å, $\alpha = \gamma = 90°$ and $\beta \approx 107°$ (Supplementary Note 1), belonging to the $TMPX_3$ family (TM: transition metal, X: S/Se)[24–30]. For the non-HE individual $TMPX_3$ members, as shown in Fig. 1a–d, $MnPS_3$ exhibits Néel-type magnetic order with a propagation vector $\mathbf{k} = (0, 0, 0)$, while $FePS_3$, $CoPS_3$, and $NiPS_3$ display zigzag antiferromagnetic (AFM) order with a propagation vector $\mathbf{k} = (0, 1, L)$ where L varies with the specific TM element (Table 1). The magnetic moments in these materials are confined to the ac^* plane (Fig. 1e), and their precise orientations are also element-dependent (Table 1). Here, **a, b**, and **c** represent the real-space vectors, while $\mathbf{a}^*$ $\mathbf{b}^*$, and $\mathbf{c}^*$ denote reciprocal vectors. Note that $\mathbf{c}^*$ is orthogonal to **a**, and $\mathbf{b}^*$ is parallel to **b**. For $HEPS_3$, which incorporates four different TM elements in equal concentrations, long-range magnetic order is hinted by magnetic susceptibility measurements at low temperatures[11], presenting a unique instance of magnetic order within a highly disordered system. Furthermore, the availability of $HEPS_3$ single crystals enables detailed exploration of its magnetic properties.

Here, combining neutron diffraction and resonant soft x-ray scattering (RSXS) techniques, we have comprehensively investigated the magnetic ordering in $HEPS_3$ single crystals. Neutron diffraction is a powerful tool for detecting various forms of magnetic order, including long-range and short-range types, with greater access to reciprocal

Table 1 | Magnetic order properties of the Mn, Fe, Co, and Ni ions in $HEPS_3$ and non-HE individual $TMPX_3$ compounds

Element	Mn	Fe	Co	Ni
Θ (deg) in $TMPX_3$	82	90	10	0
M (μ_B) in $TMPX_3$	4.43	4.52	3.36	1.05
k in $TMPX_3$	(0, 0, 0)	(0, 1, 0.5)	(0, 1, 0)	(0, 1, 0)
T_N (K) in $TMPX_3$	78	118	120	155
	Ref. 41	Ref. 31	Ref. 42	Ref. 43
Θ (deg) in $HEPS_3$	35	72	32	50
M (μ_B) in $HEPS_3$	1.51 (1)			
k in $HEPS_3$	(0, 1, 0)			
T_N (K) in $HEPS_3$	72			

Here, Θ is the angle between the magnetic moment and lattice **a** direction (Fig. 1e), M is the moment magnitude determined by neutron diffraction, and **k** is the propagation vector.

space. In contrast, resonant soft x-ray scattering (RSXS), despite its limited reciprocal space coverage, achieves element-specific resolution by tuning the incident photon energy to the resonant edge of the target element. Our neutron diffraction experiments reveal the presence of three-dimensional (3D) long-range magnetic order, with a Néel temperature of $T_N \approx 72$ K, coexisting with 2D magnetic signals. RSXS measurements further confirm that all four TM elements participate in the magnetic ordering through a unified phase transition. The resulting magnetic structure features element-dependent spin orientations, attributed to the competition between single-ion anisotropies and exchange interactions.

Results

Sample characterization

First, we verify the random distribution of TM elements in $HEPS_3$ through atomic-resolved elemental mapping using scanning transmission electron microscopy (STEM) on an exfoliated $HEPS_3$ thin flake. The sample, with a thickness of dozens of unit cells, enables the STEM mapping to be interpreted as spatial averages across multiple stacked honeycomb layers. As shown in Fig. 1f, the images reveal a homogeneous intensity distribution for each element, indicating that all elements are randomly distributed throughout the lattice. While a high-entropy scenario is well established, an anomaly indicative of magnetic phase transition is observed in the magnetic susceptibility measurements of $HEPS_3$ at $T_N = T_1 \approx 72$ K, followed by another transition taking place at $T_2 \approx 40$ K, below which the zero-field-cooling (ZFC) and field-cooling (FC) profiles split (Fig. 1g). This second transition likely originates from glassy behaviors or spin reorientations (Supplementary Note 2). Note that T_N observed in $HEPS_3$ is very close to that of non-HE $MnPS_3$ ($T_N \approx 78$ K, see Table 1). Above 80 K, the susceptibility follows Curie-Weiss behavior with a Curie-Weiss temperature of -43 K and an effective moment of 3.03 μ_B/site, corresponding to a saturated moment of 2.19 μ_B/site assuming a g-factor of 2 (Supplementary Note 2). Intriguingly, in binary or ternary $TMPX_3$ compounds, where disorder is expected to be less significant than in $HEPS_3$, the anomaly related to T_1 is more rounded, suggesting reduced correlation lengths (Fig. 1g). This observation underscores the importance of high configurational entropy in stabilizing the long-range magnetic order in $HEPS_3$.

Neutron diffraction

To elucidate the origin of the magnetic susceptibility anomaly at T_1, we conducted neutron diffraction measurements on $HEPS_3$ single crystals. At 6 K, additional Bragg peaks can be observed in the diffraction patterns alongside structural nuclear peaks that are also available at 250 K, demonstrating the emergence of magnetic order (Fig. 2a–d). These magnetic reflections can be described by a single propagation vector **k** = (0, 1, 0), with three equivalent domains arising from the honeycomb lattice within each van der Waals layer[31]. Detailed examination of the H and K dependence reveals that the in-plane magnetic peak widths are comparable to those of the nuclear reflections, confirming the establishment of long-range order (Fig. 2e, f). In contrast, along the L direction, in addition to the sharp peaks corresponding to 3D magnetic order, diffuse scattering is also observed (Fig. 2d, g), suggesting the simultaneous presence of 2D magnetic order. Note that the in-plane **k** vector is identical for both 3D and 2D magnetic signals, implying that the 2D signals maintain the same in-plane spin configuration and correlation characteristics as the 3D ones. The primary distinction between the 2D and 3D magnetic order is the reduced interlayer correlations. For the 3D magnetic order, adjacent layers are strongly coupled with parallel alignment of magnetic moments between neighboring planes. In contrast, the 2D magnetic order exhibits reduced or essentially decoupled layers, where the spin arrangement in one layer weakly affects neighboring layers. While stacking faults may play a role here, they cannot completely explain the observed 2D signals (Supplementary Note 3).

Regarding the temperature dependence, the intensity of the 3D magnetic signals decreases with increasing temperature, and a phase transition takes place at $T_N \approx 72$ K (Fig. 2h), consistent with the susceptibility measurements. The temperature dependence was fitted using $I - \mathrm{BG} \propto (T_N - T)^{2\beta}$ (BG: background), yielding a critical exponent $\beta = 0.40(5)$. Meanwhile, the 2D magnetic signals remain detectable above T_N, persisting weakly at 90 K (Fig. 2g) before vanishing around that temperature (Fig. 2h). Through a global magnetic refinement of the 3D signals (Supplementary Note 4), we determined the preliminary spin structure of $HEPS_3$, which exhibits zigzag magnetic order with $\Theta = 49°$, where Θ denotes the angle between spin moment and lattice $\boldsymbol{a}$ direction (Fig. 2i). The refined moment magnitude is 1.51(1) μ_B/site, much smaller than the average value of the non-HE individual counterparts (Table 1). The reduced moment is partially attributed to the presence of 2D magnetic signals, which account for a substantial portion of the spectral weight. To make a quantitative estimation of the total static moment, we integrated the intensity of **Q** = (0, 1, 0) over L between -0.5 and 0.5, capturing both the 2D and 3D contributions (Fig. 2g). We find that the 3D signal spectral weight, obtained by fitting with a Gaussian profile, accounts for 67% of the total spectral weight. Since neutron diffraction intensity is proportional to the squared static moment, we estimate the total static moment to be around 1.85 μ_B/site, slightly smaller than that derived from the magnetic susceptibility (2.19 μ_B/site). The discrepancy may arise from fluctuating moments or element-specific spin orientations, which will be discussed subsequently. Overall, these analyses suggest that the long-range order is mostly homogeneous across the sample.

Resonant soft X-ray scattering

While the long-range magnetic order in $HEPS_3$ is confirmed by neutron diffraction, the microscopic properties, particularly the behaviors of individual TM elements, remain unclear. Note that neutron diffraction averages contributions from disordered elements, masking element-specific magnetic properties. To overcome this limitation, we employed RSXS measurements at the TM L edges, during which process $2p$ core electrons are resonantly excited to $3d$ valence orbitals and then de-excite[32]. By tuning incident photon energy to the resonance edge of the target element, we can selectively probe the magnetic signals of a specific element in the samples. This is evident in the x-ray absorption spectrum (XAS) data, which also reveals that all TM elements in $HEPS_3$ adopt a divalent state (Supplementary Fig. 11). Moreover, as the $HEPS_3$ sample is very thin with an ab cleavage surface, 3D magnetic signals at **Q** = (0, 1, 0) were inaccessible. However, we successfully resolved 2D magnetic signals at **Q** = (0, 1, L) with finite L (Fig. 3a).

Figure 3b–e depict the RSXS scans across the 2D magnetic signals for each TM element in $HEPS_3$. These scans reveal well-defined peak-like structures centered around $K = 1$ at low temperatures, which

https://doi.org/10.1038/s41467-026-70184-x

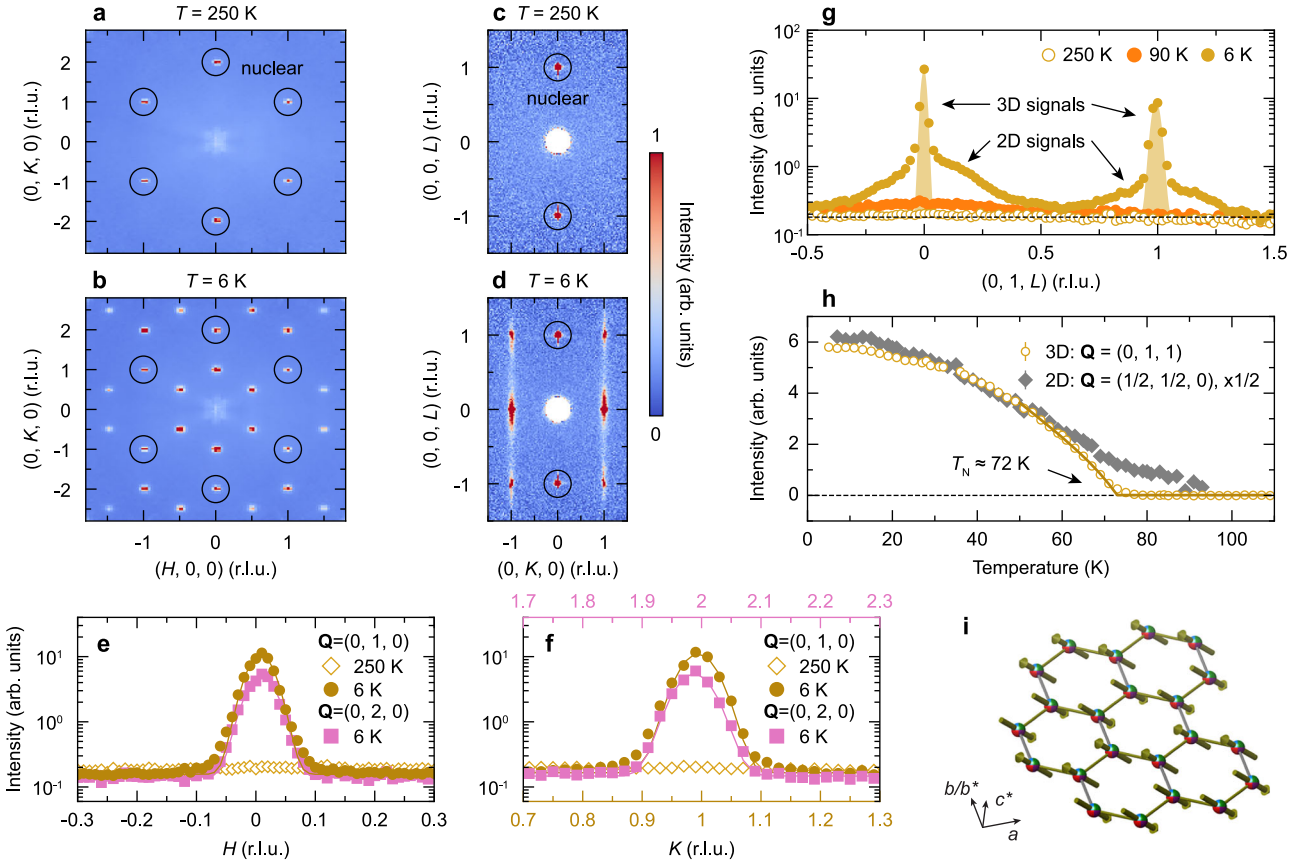

Fig. 2 | Neutron diffraction measurements on $HEPS_3$ single crystals. a, **b** Neutron diffraction patterns in the *HK*0 plane collected at 250 K and 6 K, respectively, with *L* integrated in the range of [-0.2, 0.2]. **c**, **d** Neutron diffraction patterns in the 0*KL* plane. The black circles highlight the nuclear peaks. **e**, **f** One-dimensional **Q** cuts along *H* and *K* directions, respectively, across the nuclear [**Q** = (0, 2, 0)] and magnetic reflections [**Q** = (0, 1, 0)] at the indicated temperatures. The solid lines are fits with Gaussian profiles, yielding FWHM (in unit of r.l.u.) of 0.0539(6) (nuclear) and 0.0496(5) (magnetic) along *H*, and 0.070(1) (nuclear) and 0.068(1) (magnetic) along *K*. **g** **Q** cuts along *L* direction across the magnetic signals. The shaded area denotes the 3D magnetic signals, which exhibit different peak widths due to different contributions of sample mosaicity. The 250 K data are treated as a background reference. Note that the intensities are presented on a log scale. **h** Temperature dependence of the integrated intensities of 3D magnetic signals at **Q** = (0, 1, 1) and 2D magnetic signals at **Q** = (0.5, 0.5, 0), which corresponds to **Q** = (0, −1, 1/6) in another domain[31]. The solid line is a fit to $I - \mathrm{BG} \propto (T_N - T)^{2\beta}$ (BG: background), and the dashed line is a guide for the eye. **i** Schematic of the spin structure derived from the neutron diffraction refinements with Θ = 49°, which can be regarded as an average result over all the TM elements. All the data were collected at CORELLI, including the temperature dependence. r.l.u., reciprocal lattice units.

disappear as the temperature increases, consistent with the magnetic phase transition. The magnetic signals of Ni exhibit sharper peak profiles (Fig. 3e, see also Supplementary Fig. 10). However, it should be noted that **Q** resolution varies for different elements due to the various incident energy, penetration depth, and beam footprint. A detailed investigation of the temperature-dependent RSXS signals shows a unified magnetic phase transition, whose behaviors are in good agreement with the neutron diffraction measurements on the 2D signals (Fig. 3f). This suggests that all TM elements in $HEPS_3$ undergo a simultaneous magnetic phase transition at the same temperature. Note that the amplitudes of the magnetic signals are affected by multiple factors, including the azimuthal angle, incident photon energy, number of electrons in the valence band, and self-absorption effects, making direct intensity comparisons between elements unreliable. While XAS data exhibit negligible linear dichroism for all four TM elements (Supplementary Fig. 11), their magnetic signals show distinct polarization-dependent energy profiles (Fig. 3g–j). Given the strong RSXS cross-section dependence on spin orientation, these distinct behaviors imply different spin orientations for each element.

To verify these observations and quantitatively determine the spin orientations of each TM element in $HEPS_3$, we examined the azimuthal dependence of the 2D magnetic signals by rotating the sample about the **Q** vector (Fig. 3a). Upon rotation, the cross-sectional profile of the magnetic RSXS signals changes for both polarization channels[33,34]. As shown in Fig. 4, each TM element displays unique azimuthal intensity modulations, directly indicating distinct spin orientations even without theoretical modeling. Although the azimuthal scan range is restricted by hardware limitations, we can model the intensity modulation by assuming that the spin moments rotate within the ac^* plane. This assumption is validated by the observed spin structures in the non-HE $TMPX_3$ counterparts and the aforementioned neutron diffraction measurements on $HEPS_3$. By simultaneously fitting the azimuthal dependence in both polarization channels (Methods), we derived the best fit for each TM element, the results of which are presented in Fig. 4. The resulting inclined angles, Θ, vary among elements and deviate from those observed in the non-HE $TMPX_3$ materials (Table 1). Notably, the average Θ across the four TM elements (47°) closely matches the neutron refinement result (49°), highlighting the consistency between neutron and RSXS measurements. Furthermore, the element-specific spin orientation may contribute to the reduced net spin moment derived from neutron diffraction refinement, an analysis that is based on an average spin structure.

Discussion

Combining neutron diffraction and RSXS results, we establish a comprehensive picture of the magnetic order in $HEPS_3$, as schematically

https://doi.org/10.1038/s41467-026-70184-x

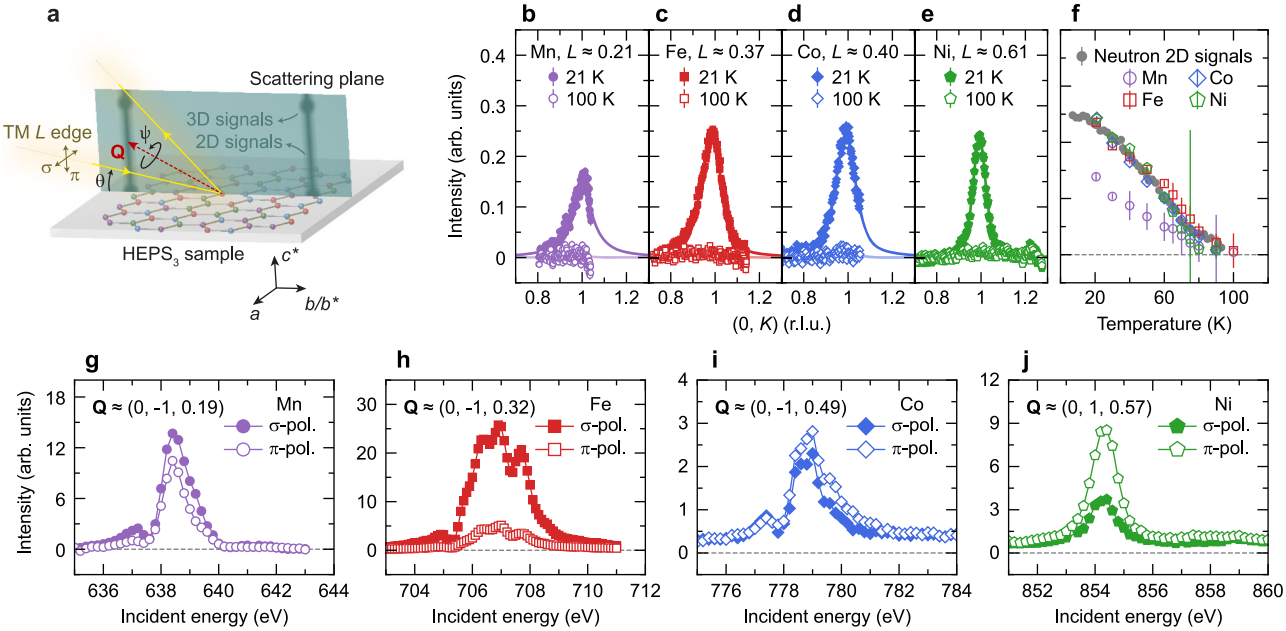

Fig. 3 | Resonant soft x-ray scattering (RSXS) measurements on $HEPS_3$. **a** Schematic diagram of the RSXS experiment setup. Note that θ is the sample angle and ψ is the azimuthal angle. Negative K is defined for grazing-incidence conditions. The polarization of the outgoing photons is not distinguished. **b**–**e** Background subtracted RSXS scans across the 2D magnetic signals at the indicated temperatures for each TM element. The solid curves are fits using pseudo-Voigt profiles. **f** Temperature dependence of the fitted peak heights of different elements, indicating a unified magnetic transition. The neutron 2D signals are the same as in Fig. 2h. All error bars represent 1 standard deviation. **g**–**j** Background subtracted fix-**Q** energy dependence of the 2D magnetic signals for each TM element in $HEPS_3$ with different incident photon polarizations. Data presented in (**b**–**f**) were collected at REIXS beamline with π polarization, and data in **g**–**j** were collected at 13-3 beamline at 12 K with $\psi \approx 0^{\circ}$.

illustrated in Fig. 1h. On a large scale, long-range zigzag AFM order is stabilized at low temperatures, resembling $FePS_3$, $CoPS_3$, and $NiPS_3$, but contrasting with $MnPS_3$, which exhibits Néel-type magnetic order. Given that the exchange interactions of $MnPS_3$ are the weakest among the four non-HE individual $TMPX_3$ compounds[28,35–40], it is very likely that the Néel-type magnetic order is disrupted and the Mn atoms in $HEPS_3$ are compelled to adopt a zigzag spin arrangement due to stronger exchange interactions with other transition metals.

At the local level, each TM element in $HEPS_3$ adopts a preferential spin orientation governed by single-ion anisotropy, which is shaped by the ionic environment, electronic hoppings, and potentially spin-orbit coupling. Based on the magnetic structure and spin dynamics of $TMPX_3$ probed by neutron scattering, it is concluded that Fe^{2+} and Co^{2+} ions exhibit robust easy-axis and easy-plane anisotropy, respectively, while Mn^{2+} and Ni^{2+} ions are mostly isotropic[28,31,36,37,39,41–43]. This is due to their different d-orbital occupations. For Mn^{2+} and Ni^{2+} ions, which have half-filled $3d$ and e_g shells, respectively, orbital degrees of freedom are mostly quenched, leading to negligible anisotropy, whereas Fe^{2+} and Co^{2+} ions tend to exhibit robust but distinct anisotropy due to combined spin-orbit coupling and trigonal distortion (Supplementary Note 5).

Exchange interactions, however, promote parallel spin alignment to minimize the total energy, creating a strong competition with single-ion anisotropy. This interplay generates a novel frustration mechanism, distinct from the more commonly discussed geometric frustration[44]. If exchange interactions were negligible, various elements would retain their intrinsic anisotropy, whereas dominant exchange interactions would impose a uniform spin orientation (Fig. 1i). In $HEPS_3$, an intermediate scenario prevails, giving rise to a synergic magnetic order where each TM element adopts a spin orientation that reflects a compromise between local anisotropy and exchange interactions, deviating from the ones observed in the non-HE $TMPX_3$ analogs (Table 1). This competition can be illustrated by a toy model, which demonstrates how spin orientations are tuned by the anisotropy-to-interaction ratio (Supplementary Note 6). Note that the single-ion anisotropy is least profound for Mn^{2+} and Ni^{2+}, making their spin orientations less resistant to competition with exchange interactions.

The observed spin structure represents an exotic, new type of magnetic ordering that is synergically established by different TM elements in a highly disordered system. It features a long-range coherent magnetic pattern, where spin moments from various TM elements are arranged in a zigzag AFM fashion and collectively participate in a unified magnetic phase transition. While the order parameter might have a form deviated from conventional ones, it remains detectable through neutron diffraction and RSXS measurements. It would also be insightful to see how it responds to local probes such as nuclear magnetic resonance (NMR) or muon spin rotation/relaxation/resonance (μSR). Nevertheless, due to the random distribution of different elements, local properties – such as spin size, exchange interactions, and spin orientations – vary from site to site without a repeating pattern. Consequently, explicit periodicity is absent, precluding the definition of a conventional magnetic unit cell. Notably, RSXS can still resolve the element-specific magnetic signatures. This is supported by a toy model simulation, in which a quarter of the sites are randomly selected and occupied, and the magnetic peak at $\mathbf{Q} = (0, 1)$ is preserved, but with significantly reduced amplitude (Supplementary Note 7).

In conclusion, combining neutron diffraction and RSXS measurements, we have identified long-range magnetic order in a HE antiferromagnet $HEPS_3$, despite significant atomic disorder. The magnetic order is synergically established by four different magnetic elements—each with distinct magnetic characteristics and randomly distributed across the lattice—via a unified phase transition. This observation showcases a novel type of synergic magnetic order, devoid of periodic spin patterns, which challenges conventional understanding of magnetism and opens new avenues for engineering materials with tailored magnetic properties. Our findings highlight the complexity of HE magnets and the importance of element-specific

https://doi.org/10.1038/s41467-026-70184-x

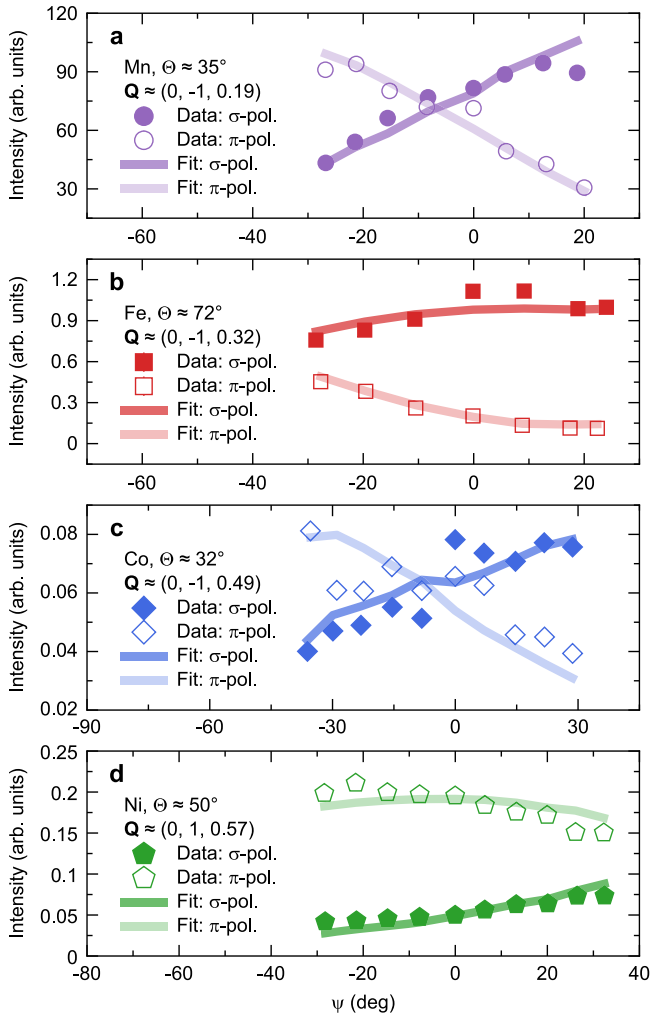

Fig. 4 | Azimuthal dependence of the 2D magnetic signals in $HEPS_3$ for each element. a–d $\psi = 0$ corresponds to the position with **Q** = (0, 1, 0) lying in the scattering plane. All the data were collected at 13-3 beamline at 12 K. Note that we use a different data processing protocol here so that the intensities are not directly comparable to Fig. 3g–j (Methods).

magnetic behavior analysis in future studies. However, several questions remain unresolved. For instance, the microscopic mechanism underlying the long-range order in such a highly disordered system, as well as the reasons behind the suppression of spin glass behaviors by high entropy, remain to be fully understood. Whether this arises from enhanced quantum fluctuations, emergent collective modes, or other fundamental processes, and what role kinetic constraints or entropic barriers play in stabilizing or destabilizing the spin glass phases, are questions that warrant further exploration. These open challenges highlight the need for advanced theoretical and experimental efforts to unravel the physics of this exotic magnetic state.

Methods

Sample synthesis and characterization

Single-crystalline $(Mn_{1/4}Fe_{1/4}Co_{1/4}Ni_{1/4})PS_3$ ($HEPS_3$) samples, as well as the binary and ternary $TMPX_3$ compounds, were grown using the chemical vapor transport (CVT) method as detailed in the previous report[11]. Atomic-resolved EDS mapping was performed using an aberration-corrected STEM (JEM NEOARM), operated at 200 kV. As mentioned in the main text, the STEM mapping is interpreted as an average result of multiple stacked honeycomb layers, leading to a triangular arrangement considering ABC stacking. Consequently, elements that are randomly distributed throughout the lattice will display uniform intensity at each site.

Neutron diffraction experiment

All neutron diffraction measurements were conducted using the CORELLI instrument at Spallation Neutron Source (SNS), Oak Ridge National Laboratory (ORNL)[45,46]. One piece of single crystal (27 mg in weight; 6 × 3 mm in size) was aligned first in the *H0L* scattering plane and subsequently in the 0*KL* scattering plane, utilizing monoclinic notation. Diffraction patterns were collected at 6 K, 90 K, and 250 K by rotating the sample with a fixed tilting angle. For the temperature dependence measurements, the sample position and orientations were unchanged; data were acquired with a 5 min counting time per temperature point with a step of 2 K.

RSXS experiments

The RSXS experiments were performed at the REIXS (10ID-2) beamline of the Canadian Light Source (CLS)[47] and 13-3 beamline of the Stanford Synchrotron Radiation Lightsource (SSRL) at the SLAC National Accelerator Laboratory[48]. Both have an in-vacuum 4-circle diffractometer to access the magnetic signals.

For the REIXS experiment, XAS data were collected using a silicon drift detector (SDD) at a fixed position, while RSXS signals were measured with another SDD equipped at the goniometer arm at the peak position of the L_3 edge for each transition-metal element in $HEPS_3$ (Supplementary Fig. 11). RSXS scans were conducted by rotating the sample at a fixed scattering angle 2θ, considering that the signal is independent of L within a small range. The x-ray energies were chosen to be 639.3 eV, 706.9 eV, 777.7 eV, and 851.9 eV for the Mn, Fe, Co, and Ni L_3 edges, respectively. The intensity was normalized to the incoming x-ray flux. Background subtraction was performed using high-temperature data for all RSXS scans (Supplementary Fig. 12).

In the 13-3 experiment, a 2D CCD detector was employed, covering a finite range of **Q**. The collected signals were normalized by electron current. In Fig. 4, the data were further normalized by fluorescence to account for variations in measurement efficiency, particularly due to self-absorption effects and changes in the x-ray footprint on the sample, which is not relevant in the energy dependence presented in Fig. 3g–j. Furthermore, for the energy-dependent measurements, all diffraction angles, including the scattering angle 2θ, were fixed. Although **Q** varies slightly with energy, the large area of the CCD detector ensured that magnetic signals were still captured, enabling equivalent fix-**Q** energy scans. The azimuthal-dependent measurements shown in Fig. 4 were conducted at the peak position of the L_3 edge (Supplementary Fig. 13). To be more specific, the x-ray energies are 638.4 eV, 707 eV, 779 eV, and 853.9 eV for the Mn, Fe, Co, and Ni L_3 edges, respectively. For each azimuthal angle, a RSXS scan was performed by rotating the sample. The magnetic signals in the *HK* plane were fitted with a 2D Lorentzian function to determine the peak height. The signals along the L direction were averaged as they exhibited no significant dependence on L within the small L range investigated.

Simulation of the azimuthal dependence

Considering that the linear dichroism is negligible in $HEPS_3$, we use a simplified model based on spherical symmetry to simulate the azimuthal dependence of the magnetic signals:

$$\mathcal{F} = \kappa \cdot \boldsymbol{\epsilon} \times \boldsymbol{\epsilon}' \cdot \mathbf{M} \tag{1}$$

where κ is a scale factor, $\boldsymbol{\epsilon}$ and $\boldsymbol{\epsilon}'$ are the incident and emission photon polarization, respectively, and **M** is the spin moment. The magnetic RSXS cross-section can be obtained as $\mathcal{I} = \mathcal{F}^2$. **M** is confined within the ac^* plane and the fitting results are presented in Fig. 4. Note that for each element, a unified scale factor κ is used for different polarizations. The outgoing photon polarization is not distinguished. Thus, the

simulated signals are summed over two polarization channels, σ' and π', for the outgoing photons. Note that magnetic signals will contribute to the σ-π', π-π', and π-σ' channels but not σ-σ' channel. The full-range calculation results for the azimuthal dependence are presented in Supplementary Fig. 14, which are simulated based on calculated motor positions, while for Fig. 4, experimental motor positions are used. The discrepancy is negligible.

Data availability

All data that support the findings of this study have been deposited in the Zenodo database with the access code 17636716[49].

References

1. Binder, K. & Young, A. P. Spin glasses: Experimental facts, theoretical concepts, and open questions. *Rev. Mod. Phys.* **58**, 801 (1986).
2. Mydosh, J. A. Spin glasses: redux: an updated experimental/materials survey. *Rep. Prog. Phys.* **78**, 052501 (2015).
3. Yeh, J.-W. et al. Nanostructured high-entropy alloys with multiple principal elements: novel alloy design concepts and outcomes. *Adv. Eng. Mater.* **6**, 299 (2004).
4. Miracle, D. B. & Senkov, O. N. A critical review of high entropy alloys and related concepts. *Acta Materialia* **122**, 448 (2017).
5. Ding, Q. et al. Tuning element distribution, structure and properties by composition in high-entropy alloys. *Nature* **574**, 223 (2019).
6. George, E. P., Raabe, D. & Ritchie, R. O. High-entropy alloys. *Nat. Rev. Mater.* **4**, 515 (2019).
7. Sun, L. & Cava, R. J. High-entropy alloy superconductors: Status, opportunities, and challenges. *Phys. Rev. Mater.* **3**, 090301 (2019).
8. Oses, C., Toher, C. & Curtarolo, S. High-entropy ceramics. *Nat. Rev. Mater.* **5**, 295 (2020).
9. Rost, C. M. et al. Entropy-stabilized oxides. *Nat. Commun.* **6**, 8485 (2015).
10. Witte, R. et al. High-entropy oxides: An emerging prospect for magnetic rare-earth transition metal perovskites. *Phys. Rev. Mater.* **3**, 034406 (2019).
11. Ying, T. et al. High-entropy van der Waals materials formed from mixed metal dichalcogenides, halides, and phosphorus trisulfides. *J. Am. Chem. Soc.* **143**, 7042 (2021).
12. Ying, T., Yu, T., Qi, Y., Chen, X. & Hosono, H. High entropy van der Waals materials. *Adv. Sci.* **9**, 2203219 (2022).
13. Chen, X. et al. Insulator-metal-superconductor transition in the medium-entropy van der Waals compound MPSe$_3$ (M=Fe, Mn, Cd, and In) under high pressure. *Phys. Rev. B* **106**, 184502 (2022).
14. Laha, A. et al. High-entropy engineering of the crystal and electronic structures in a Dirac material. *Nat. Commun.* **15**, 3532 (2024).
15. Sarkar, A. et al. High entropy oxides for reversible energy storage. *Nat. Commun.* **9**, 3400 (2018).
16. Schweidler, S. et al. High-entropy materials for energy and electronic applications. *Nat. Rev. Mater.* **9**, 266 (2024).
17. Han, L. et al. Multifunctional high-entropy materials. *Nat. Rev. Mater.* **9**, 846 (2024).
18. Yin, Y. et al. Spin-glass behavior and magnetocaloric properties of high-entropy perovskite oxides. *Appl. Phys. Lett.* **120**, 082404 (2022).
19. Angelo, G. et al. Absence of long-range magnetic ordering in a trirutile high-entropy oxide ($Mn_{0.2}Fe_{0.2}Co_{0.2}Ni_{0.2}Cu_{0.2}$)$Ta_{1.92}O_{6-\delta}$. *Inorg. Chem.* **64**, 3196 (2025).
20. Johnstone, G. H. J. et al. Entropy engineering and tunable magnetic order in the spinel high-entropy oxide. *J. Am. Chem. Soc.* **144**, 20590 (2022).
21. Zhu, L. et al. Antiferromagnetism and phase stability of CrMnFeCoNi high-entropy alloy. *Phys. Rev. Lett.* **133**, 126701 (2024).
22. Min, L. et al. High entropy protected sharp magnetic transitions in highly disordered spinel ferrites. *J. Am. Chem. Soc.* **146**, 24320 (2024).
23. Nalbandyan, V. B. et al. Preparation and characterization of a high-entropy magnet, (Mg, Mn, Co, Ni, Cu)$_3$TeO$_6$. *Inorg. Chem.* **63**, 22372 (2024).
24. Zhou, F. et al. Dynamical criticality of spin-shear coupling in van der Waals antiferromagnets. *Nat. Commun.* **13**, 6598 (2022).
25. Matthiesen, M. et al. Controlling magnetism with light in a zero orbital angular momentum antiferromagnet. *Phys. Rev. Lett.* **130**, 076702 (2023).
26. Zong, A. et al. Spin-mediated shear oscillators in a van der Waals antiferromagnet. *Nature* **620**, 988 (2023).
27. Ilyas, B. et al. Terahertz field-induced metastable magnetization near criticality in FePS$_3$. *Nature* **636**, 609 (2024).
28. Wildes, A. R. et al. Spin wave spectra of single crystal CoPS$_3$. *Phys. Rev. B* **107**, 054438 (2023).
29. Kang, S. et al. Coherent many-body exciton in van der Waals antiferromagnet NiPS$_3$. *Nature* **583**, 785 (2020).
30. He, W. et al. Magnetically propagating Hund's exciton in van der Waals antiferromagnet NiPS$_3$. *Nat. Commun.* **15**, 3496 (2024).
31. Lançon, D. et al. Magnetic structure and magnon dynamics of the quasi-two-dimensional antiferromagnet FePS$_3$. *Phys. Rev. B* **94**, 214407 (2016).
32. Fink, J., Schierle, E., Weschke, E. & Geck, J. Resonant elastic soft x-ray scattering. *Rep. Prog. Phys.* **76**, 056502 (2013).
33. Grenier, S. & Joly, Y. Basics of resonant elastic x-ray scattering theory. *J. Phys.: Conf. Ser.* **519**, 012001 (2014).
34. Sears, J. A. et al. Ferromagnetic Kitaev interaction and the origin of large magnetic anisotropy in α-RuCl$_3$. *Nat. Phys.* **16**, 837 (2020).
35. Kurosawa, K., Saito, S. & Yamaguchi, Y. Neutron diffraction study on MnPS$_3$ and FePS$_3$. *J. Phys. Soc. Jpn.* **52**, 3919 (1983).
36. Liao, J. et al. Spin and lattice dynamics in the van der Waals antiferromagnet MnPSe$_3$. *Phys. Rev. B* **109**, 224411 (2024).
37. Chen, L. et al. Thermal evolution of spin excitations in honeycomb Ising antiferromagnetic FePSe$_3$. *npj Quantum Mater.* **9**, 40 (2024).
38. Kim, C. et al. Spin waves in the two-dimensional honeycomb lattice XXZ-type van der Waals antiferromagnet CoPS$_3$. *Phys. Rev. B* **102**, 184429 (2020).
39. Wildes, A. R. et al. Magnetic dynamics of NiPS$_3$. *Phys. Rev. B* **106**, 174422 (2022).
40. Scheie, A. et al. Spin wave Hamiltonian and anomalous scattering in NiPS$_3$. *Phys. Rev. B* **108**, 104402 (2023).
41. Ressouche, E. et al. Magnetoelectric MnPS$_3$ as a candidate for ferrotoroidicity. *Phys. Rev. B* **82**, 100408 (2010).
42. Wildes, A. R., Simonet, V., Ressouche, E., Ballou, R. & McIntyre, G. J. The magnetic properties and structure of the quasi-two-dimensional antiferromagnet CoPS$_3$. *J. Phys.: Condens. Matter* **29**, 455801 (2017).
43. Wildes, A. R. et al. Magnetic structure of the quasi-two-dimensional antiferromagnet NiPS$_3$. *Phys. Rev. B* **92**, 224408 (2015).
44. Balents, L. Spin liquids in frustrated magnets. *Nature* **464**, 199 (2010).
45. Rosenkranz, S. & Osborn, R. Corelli: Efficient single crystal diffraction with elastic discrimination. *Pramana J. Phys.* **71**, 705 (2008).
46. Ye, F., Liu, Y., Whitfield, R., Osborn, R. & Rosenkranz, S. Implementation of cross correlation for energy discrimination on the time-of-flight spectrometer CORELLI. *J. Appl. Crystallogr.* **51**, 315 (2018).
47. Hawthorn, D. G. et al. An in-vacuum diffractometer for resonant elastic soft X-ray scattering. *Rev. Sci. Instrum.* **82**, 073104 (2011).
48. Kuo, C.-T. et al. Introducing new resonant soft X-ray scattering capability in SSRL. *Rev. Sci. Instrum.* **96**, 063902 (2025).
49. Shen, Y. et al. Long-range magnetic order with disordered spin orientations in a high-entropy antiferromagnet. https://doi.org/10.5281/zenodo.17636716 (2025).

Acknowledgements

We thank Gang Chen for inspiring discussions. This work was supported by the National Key R&D Program of China (Grant No. 2024YFA1408301

(Y.S.), 2023YFA1406500 (J.W.), 2021YFA1400300 (Y.L.)) and the National Natural Science Foundation of China (Grant No. 12574139 (Y.S.), 12425403 (Y.L.), 52272267 (T.Y.), 52522201 (T.Y.), 12261131499(Y.L.)). Neutron diffraction measurements of this research used resources at the Spallation Neutron Source (SNS), a US Department of Energy Office of Science User Facility operated by the Oak Ridge National Laboratory (ORNL). The beam time was allocated to CORELLI on Proposal No. IPTS-30179.1. RSXS measurements were carried out at the Stanford Synchrotron Radiation Lightsource (SSRL), SLAC National Accelerator Laboratory, which is supported by the US Department of Energy, Office of Science, Office of Basic Energy Sciences (contract No. DE-AC02-76SF00515), and the Canadian Light Source (CLS), a national research facility of the University of Saskatchewan, which is supported by the Canada Foundation for Innovation (CFI), the Natural Sciences and Engineering Research Council (NSERC), the Canadian Institutes of Health Research (CIHR), the Government of Saskatchewan, and the University of Saskatchewan. Notice: This manuscript has been authored by UT-Battelle, LLC, under contract DE-AC05-00OR22725 with the US Department of Energy (DOE). The US government retains and the publisher, by accepting the article for publication, acknowledges that the US government retains a nonexclusive, paid-up, irrevocable, worldwide license to publish or reproduce the published form of this manuscript or allow others to do so, for US government purposes. DOE will provide public access to these results of federally sponsored research in accordance with the DOE Public Access Plan (https://www.energy.gov/doe-public-access-plan).

Author contributions

Y.S., J.W., and T.Y. conceived the project. Q.Z., Y.Z., and T.Y. synthesized and characterized the samples. X.G., F.Y., and J.W. performed the neutron measurements. Y.S., G.Z., H.L., C.T.K., J.S.L., and R.S. performed the X-ray measurements. Y.S., Z.P., X.Q., J.W., T.Y., and Y.L. interpreted the data. The paper was written by Y.S., J.W., and T.Y. with input from all co-authors.

Competing interests

The authors declare no competing interests.

Additional information

Supplementary information The online version contains supplementary material available at https://doi.org/10.1038/s41467-026-70184-x.

Correspondence and requests for materials should be addressed to Yao Shen, Jinchen Wang or Tianping Ying.

Peer review information *Nature Communications* thanks the anonymous, reviewers for their contribution to the peer review of this work. A peer review file is available.